SPIN STRUCTURE FUNCTION MEASUREMENTS FROM E143 AT SLAC

H. R. Band*
University of Wisconsin
Madison, WI 53706

Representing the E143 Collaboration

ABSTRACT

Recent high statistics measurements of the nucleon spin structure functions by the E143 Collaboration are presented. The structure functions g_1^p and g_1^d have been measured over the range $0.029 < x < 0.8$ and $1.3 < Q^2 < 10$ (GeV/c)^2 using deep inelastic scattering of polarized electrons from polarized ammonia and deuterated ammonia targets. Evaluation of the integral $\Gamma_1^p = \int_0^1 g_1^p(x,Q^2)dx$ at fixed $Q^2 = 3$ (GeV/c)^2 yields $0.127 \pm 0.004 \pm 0.010$, in agreement with previous experiments, but well below the Ellis-Jaffe sum rule prediction of 0.160 ± 0.006. The integral $\Gamma_1^d = \int_0^1 g_1^d(x,Q^2)dx$ also evaluated at fixed Q^2=3 (GeV/c)^2 gives $0.041 \pm 0.004 \pm 0.004$, again below the Ellis-Jaffe sum rule prediction of 0.068 ± 0.005. From g_1^p and g_1^d, the neutron structure function g_1^n can be computed with Γ_1^n measured as $-0.037 \pm 0.008 \pm 0.010$. Combined with the measurement of g_1^p, we find $\Gamma_1^p - \Gamma_1^n = 0.163 \pm 0.010 \pm 0.016$ which agrees with the prediction of the Bjorken sum rule with $O(\alpha_s^3)$ corrections, $\Gamma_1^p - \Gamma_1^n = 0.171 \pm 0.008$. In the quark-parton model, this implies that the net helicity carried by the quarks is $\Delta q = 0.34 \pm 0.04$.

*Supported by DOE Contract DE-AC02-76ER00881.

1 Spin Structure Functions

1.1 Introduction

The E143 experiment is the latest SLAC fixed-target experiment to measure nucleon spin structure functions with polarized electron beams. The pioneering spin structure measurements were SLAC E80 in 1976[1] and E130 in 1983[2] which used cryogenic butanol targets to measure the proton polarized structure function $g_1(x)$ over a range in the Bjorken scaling variable, x, of 0.1 to 0.65. These experiments were motivated by the quark-parton model which described the unpolarized deep inelastic scattering data and by the expectation of large asymmetries in polarized nucleon scattering. Predictions of the integral of g_1 had been derived from current algebra by Bjorken.[3] The Bjorken sum rule predicts the difference $\Gamma_1^p - \Gamma_1^n = \frac{1}{6}(g_A/g_V)$ at infinite Q^2 where $\Gamma_1^p = \int_0^1 g_1^p(x,Q^2)dx$ for the proton, $\Gamma_1^n = \int_0^1 g_1^n(x,Q^2)dx$ for the neutron, and g_A and g_V are the nucleon axial–vector and vector coupling constants. QCD corrections evolve the sum rule to the finite Q^2 reachable by experiment and make the sum rule a basic prediction of QCD. Ellis and Jaffe,[4] assuming SU(3) flavor symmetry and an unpolarized strange sea, later made predictions for the proton and neutron integrals individually which together satisfied the Bjorken sum rule. Within the large measurement errors, the data from E80 and E130 agreed with the Ellis-Jaffe predictions.

In 1988, the CERN EMC experiment using 100–200 GeV muon beams to reach low x values reported surprising results on g_1^p.[5] Although consistent with the SLAC experiments over the common x range, EMC found that g_1 was smaller than expected in the x range below 0.2 and that Γ_1^p disagreed significantly with the Ellis-Jaffe sum rule. Since in the quark-parton model Γ_1^p is related to the integral over the quark spin distributions, the fraction of the proton spin carried by the quarks was measured as $\Delta q = 0.14 \pm 0.23$ with a strange quark contribution of $\Delta s = -0.22 \pm 0.09$. Popularly known as the "Spin Crisis," these results generated much theoretical speculation and debate, as well as prompting the current generation of experiments.

The CERN SMC experiment in 1993[6] reported results on the deuteron which again disagreed with Ellis-Jaffe predictions and were consistent with the quarks carrying no net spin $\Delta q = 0.06 \pm 0.25$. Also in 1993, the SLAC E142 experiment[7] using a polarized ^{3}He target for the first time measured g_1^n with $\Gamma_1^n =$

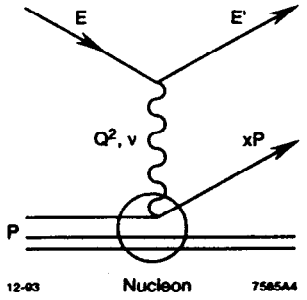

Figure 1: Variables in electron-nucleon scattering.

-0.022 ± 0.011 in agreement with the Ellis-Jaffe prediction. The total quark contribution to the nucleon spin was measured as $\Delta q = 0.57 \pm 0.11$ in disagreement with the SMC result. Combining the EMC proton and E142 neutron data, a test of the Bjorken sum rule was possible with $\Gamma_1^p - \Gamma_1^n = 0.146 \pm 0.21$ differing by 2 sigma from the predicted value of 0.187. Interpretation of the apparent discrepancies between the experiments were clouded by the differing average Q^2, x range, and analysis of the two experiments.

To clarify the experimental picture, high statistics measurements of both the proton and deuteron were proposed by E143.

1.2 Kinematics

Deep inelastic scattering experiments measure the energy E' and production angle θ of electrons scattered from an incident beam of energy E by a nucleon of mass M as shown in Fig. 1. The following scaling variables can be derived from these measured quantities:

$$Q^2 = 4EE'\sin^2[\theta/2]$$

$$x = Q^2/2M(E-E')$$

$$y = (E-E')/E.$$

In the Quark Parton Model, these variables are identified as follows: Q^2 is the four momentum of the virtual photon, x is the fraction of the nucleon momentum carried by the struck quark, and y is the fraction of of the beam energy carried by the virtual photon. The polarized spin structure functions g_1 and g_2 are related

to the experimentally measured longitudinal and transverse electron asymmetrics $A_\parallel$ and $A_\perp$ by:

$$g_1(x,Q^2) = \frac{F_1(x,Q^2)}{d}[A_\parallel + \tan(\theta/2)A_\perp] \quad (1)$$

$$g_2(x,Q^2) = \frac{F_1(x,Q^2)}{d}\frac{y}{2\sin(\theta)}\left[\frac{E+E'\cos\theta}{E'}A_\perp - \sin\theta A_\parallel\right] \quad (2)$$

where F_1 is the unpolarized structure function, $A_\parallel$ is the cross-section asymmetry between negative- and positive-helicity electron beams when the target nucleon is polarized parallel to the beam direction, and $A_\perp$ is the asymmetry when the target nucleon is polarized transverse to the beam direction. The variable d is $(1-\epsilon)(2-y)/[y(1+\epsilon R)]$ where $\epsilon^{-1} = 1 + 2[1+(\nu^2/Q^2)]\tan^2(\theta/2)$, $\nu = E - E'$, and R is ratio of the longitudinal and transverse virtual photon cross sections.

1.3 Sum Rules

The sum rule originally derived by Bjorken[3] is

$$\Gamma_1^p - \Gamma_1^n = \int (g_1^p(x) - g_1^n(x))\,dx = \frac{1}{6}\frac{g_A}{g_V} \qquad Q^2 = \infty \quad (3)$$

where g_A and g_V are nucleon axial-vector and vector couplings determined presently from β decay as $g_A/g_V = 1.2573 \pm 0.003$ (Ref. 8). QCD corrections[9] multiply $g_A/(6g_V)$ by a factor c_1 calculated to order α^3:

$$c_1 = 1 - \frac{\alpha_s(Q^2)}{\pi} - 3.58\left(\frac{\alpha_s(Q^2)}{\pi}\right)^2 - 20.22\left(\frac{\alpha_s(Q^2)}{\pi}\right)^3. \quad (4)$$

For the number of contributing quark flavors, $n_f = 3$ and $\alpha_s(Q^2 = 3) \approx 0.35 \pm 0.05$[10] yields:

$$\Gamma_1^p - \Gamma_1^n = \frac{1}{6}\frac{g_A}{g_V}c_1 = 0.171 \pm 0.008. \quad (5)$$

Assuming SU(3) symmetry in hyperon decays and $\Delta s = 0$, the Ellis-Jaffe[4] sum rules with second-order corrections[11] are

$$\Gamma_1^p = \frac{c_1(F+D)}{12} + \frac{(c_1+4c_0)(3F-D)}{36} = 0.160 \pm 0.006 \quad (6)$$

$$\Gamma_1^n = -\frac{c_1(F+D)}{12} + \frac{(c_1+4c_0)(3F-D)}{36} = -0.011 \pm 0.005. \quad (7)$$

The hyperon constants $F/D = 0.575 \pm 0.016$ and $F + D = g_A/g_V$ were used to evaluate the sum rules with the singlet QCD corrections given by

$$c_0 = 1 - \frac{\alpha_s(Q^2)}{3\pi} - 0.55\left(\frac{\alpha_s(Q^2)}{\pi}\right)^2. \quad (8)$$

The Ellis-Jaffe result for the deuteron structure function g_1^d can be calculated from g_1^p and g_1^n by correcting for the small probability ω_D that the deuteron is in the D-state:[12]

$$\Gamma_1^d = 0.5(\Gamma_1^p + \Gamma_1^n)(1 - 1.5\omega_D) = 0.068 \pm 0.005. \quad (9)$$

In the quark parton model, g_1 has a simple interpretation as:

$$g_1(x) = \frac{1}{2}\sum_i e_i^2\left[q_i^\uparrow(x) - q_i^\downarrow(x)\right]$$

where $q_i^\uparrow(x)$ is the x distribution of quarks and antiquarks of flavor i whose helicity is aligned with that of the nucleon, $q_i^\downarrow$ are quarks with helicity antialigned with the nucleon, and e_i is the quark charge. With $\Delta u = q_i^\uparrow(x) - q_i^\downarrow(x)$ for u and $\bar{u}$ type quarks, and similar definitions for other quark flavors, g_1 for the proton and neutron are:

$$g_1^p = \frac{1}{18}[4\Delta u + \Delta d + \Delta s]$$

$$g_1^n = \frac{1}{18}[4\Delta d + \Delta u + \Delta s]$$

$$\Delta q = \Delta u + \Delta d + \Delta s.$$

The above equations, plus QCD corrections, give:

$$\Delta q = \left(\frac{9}{c_0}\right)\left[\Gamma_1^p - \left(\frac{(3F+D)}{18}\right)c_1\right]. \quad (10)$$

Similar expressions hold using Γ_1^n, Γ_1^d. If the Bjorken sum rule is correct, all experiments should give the same Δq. The individual quark contributions can be found using:

$$\Delta u = \frac{\Delta q}{3} + .725 \qquad \Delta d = \frac{\Delta q}{3} - 0.532 \qquad \Delta s = \frac{\Delta q}{3} - 0.193.$$

2 E143 Experiment

The E143 experiment used the SLAC polarized electron beam with energies E of 9.8, 16.2, and 29.1 GeV scattering from polarized proton and deuteron targets in End Station A (ESA) to measure g_1^p, g_2^p, g_1^d, and g_2^d in the range $1.3 < Q^2 < 10$ $(\mathrm{GeV/c})^2$ and $0.029 < x < 0.8$. The apparatus needed for these measurements include: a high-polarization long-pulse electron source, a Møller polarimeter, a cryogenic polarized ammonia target, and large solid angle spectrometers.

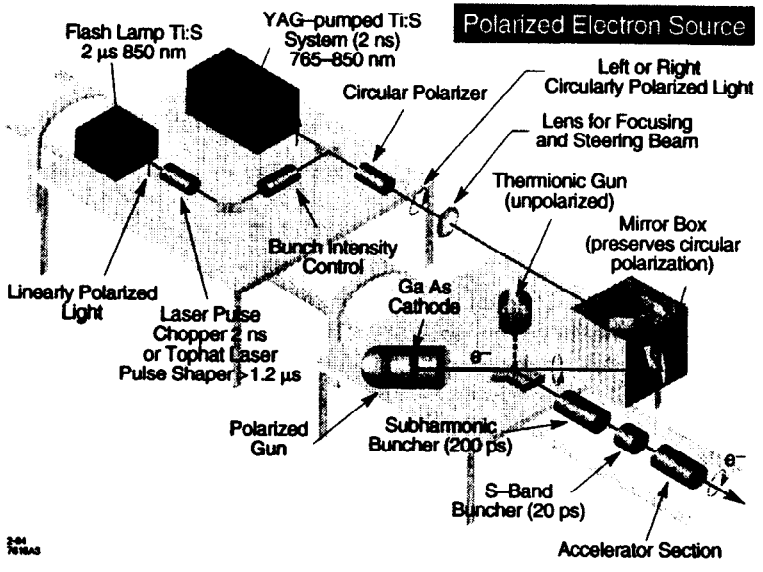

Figure 2: SLAC polarized electron source.

2.1 SLAC Polarized Beam

The SLAC polarized electron source as used for fixed target running is shown in Fig. 2. A flash-lamp-pumped Ti-sapphire laser operating at 850 nanometers illuminated a strained lattice GaAs crystal photocathode.[13] The photoemitted electrons were accelerated to high energy with no significant depolarization. The cathode is constructed from a thin strained GaAs layer grown on a five micron thick GaAsP buffer layer which in turn was grown on a 600 micron thick substrate of GaAs. The strained GaAs layer used in the photocathode was only 0.1 micron thick, yielding significantly higher beam polarizations in laboratory measurements than cathodes used in previous SLAC experiments (Fig. 3).

The polarized electron source produced beam pulses 2 μsec long at 119 Hz. Since the beam current of $2-4\times10^9$ was too low to be seen in the normal SLC beam position monitors, a second YAG-pumped Ti-sapphire laser was used to produce high intensity pulses at 1 Hz for beam position monitoring and feedback. This high current pulse was dumped before entering ESA. The helicity of each

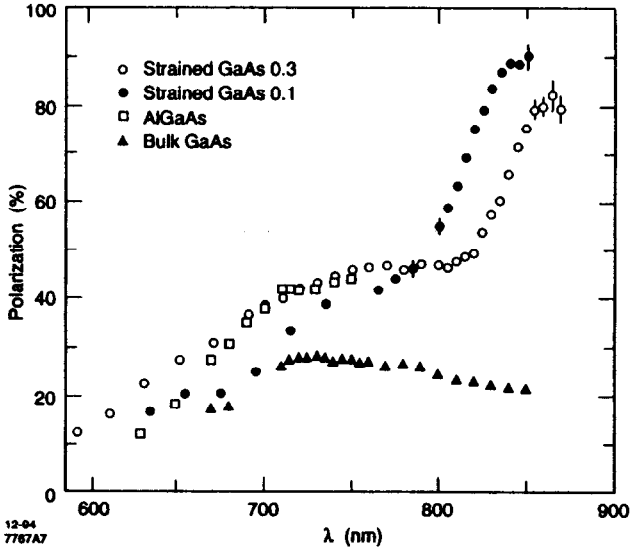

Figure 3: Beam polarization as measured in the laboratory for the four types of photocathodes used in recent SLAC polarized experiments. A bulk GaAs photocathode (SLC 1992) and an AlGaAs photocathode (E142 1992) were used to match the frequency of the flashlamp pumped dye laser used in the earlier SLAC experiments. The strained GaAs photocathodes with layer thicknesses of 0.3 micron (SLC 1993) and 0.1 micron (E143 1993) required development of YAG and flashlamp pumped Ti-Sapphire lasers.

pulse was selected randomly on a pulse-by-pulse basis to minimize instrumental asymmetries. The beam current was measured in the end station by two independent toroid systems with an uncertainty of $< 1\%$. A steering feedback system kept the average angle and position of the beam at the polarized target essentially constant. Asymmetries induced by changes in beam parameters correlated with helicity were found to be negligible throughout the experiment.

2.2 E143 Møller Polarimeter

The beam polarization was measured in ESA by a Møller polarimeter. Dedicated Møller runs took typically one hour and were made every one to two days. The E143 Polarimeter, shown in Fig. 4, differs from recent SLAC polarimeters[14] in that double-arm coincidence detectors operated in parallel with single-arm detectors.

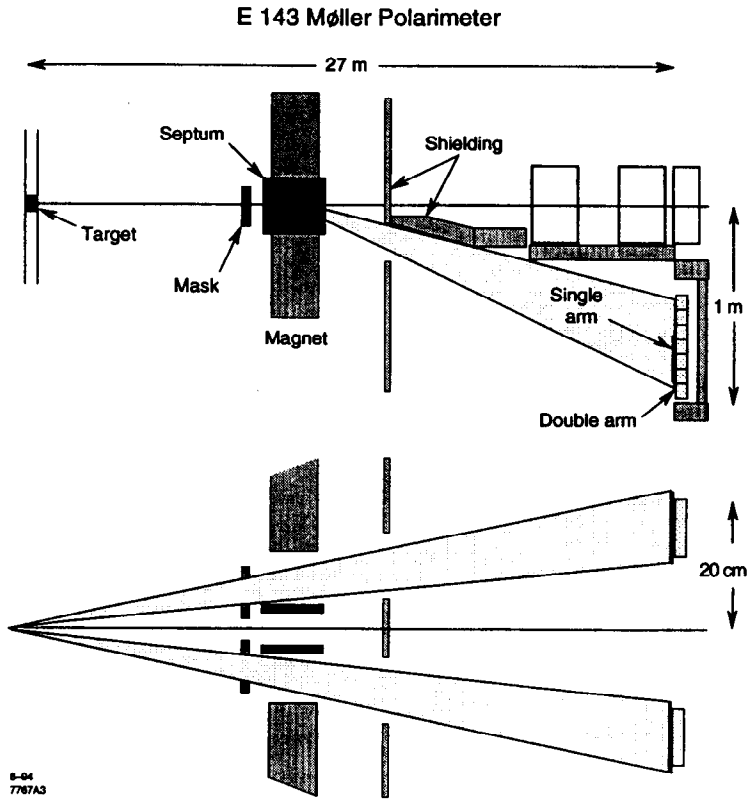

Figure 4: E143 Møller Polarimeter.

In the e^-e^- center of mass, the polarized cross section for Møller scattering[15] is

$$\frac{d\sigma}{d\Omega} = \frac{\alpha^2}{s}\frac{(3+\cos^2\theta)^2}{\sin^4\theta}[1 - P_z^B P_z^T A_z(\theta)] \tag{11}$$

and

$$A_z(\theta) = \frac{(7+\cos^2\theta)\sin^2\theta}{(3+\cos^2\theta)^2}. \tag{12}$$

Here P_z^B (P_z^T) is the beam (target) longitudinal polarization. When $\theta = 90°$, $A_z(\theta) = 7/9$ and both electrons in the lab frame have momenta ($E_{beam}/2$) and equal but opposite scattering angles. The measured asymmetry is

$$A_{meas.} = \frac{\sigma^{\uparrow\downarrow} - \sigma^{\uparrow\uparrow}}{\sigma^{\uparrow\downarrow} + \sigma^{\uparrow\uparrow}} = P_z^B P_z^T A_z(\theta), \tag{13}$$

where $\sigma^{\uparrow\uparrow}$ ($\sigma^{\uparrow\downarrow}$) is the cross section for beam and target spins aligned (anti-aligned).

Until recently, it was assumed that the Møller asymmetry was constant across the measured peak. However, it has been pointed out by Levchuk[16] that the electron orbital motion of the target foil electrons could have a significant effect on the Møller lineshape. The atomic electrons have a shell dependent momentum distribution. Electrons in the outer shells have small momenta but those from the inner shells have momenta about 100 KeV/c. Although small compared to a beam energy of 29 GeV, these momenta are not small compared to the electron rest mass and can alter the scattering angle by up to 10%. The effect causes different line shapes for scatters from different shells. Since the polarized target electrons are only in the 3d (M) shell, the fraction of signal from the polarized target electrons and thus the expected Møller asymmetry varies over the Møller scattering peak depending on the detector resolution and multiple scattering in the target material.

The polarimeter consists of a polarized electron target, a mask to select Møller scattered electrons in the vertical plane, an analyzing magnet, and both single- and double-arm detectors. The six polarized foil targets (49% Fe, 49% Co, 2% Va) are mounted at a 20° angle to the beam and placed inside a 100 Gauss magnetizing field. The foil polarization was measured to be 0.0803 for the 20 μm foils and 0.0814 for the 30, 40, and 154 μm foils with a relative systematic error of 1.7%.

A collimator downstream of the the target (Fig. 5) selects scattering angles transverse to the bend plane of the following dipole magnet. The collimator has wedge-shaped apertures of constant phi acceptance (0.2 radian top, 0.22 radian

bottom) to maintain good acceptance for Møller scattered pairs over the entire double-arm detector acceptance of 70–110° in the center of mass.

The scattered electrons exit the beam pipe and are momentum analyzed by a large aperture dipole magnet with an $\int Bdl$ of 21 kG-m. A large 3.2 inch thick septum reduces the field seen by the forward scattered beam inside the beampipe, minimizing backgrounds in the detector. Since Møller scattering is elastic, the scattered electrons have a θ-p correlation which produces a spatial $x-y$ correlation after the magnet (see Fig. 5). In Fig. 6, the position of the single- and double-arm detectors are shown relative to the Møller scattered electrons.

The single-arm detector consists of eight silicon pad detectors 12 channels wide operating in parallel behind three radiation lengths of lead. The lead convertor absorbs soft photon backgrounds and amplifies the Møller signal. Each detector accepts a specific x (momentum) range. The pad widths are large and the Møller peak is mostly contained in two channels. For this reason, corrections to the line shape for target momenta are small and change the expected Møller asymmetries in the center channels by only 3%. A signal is integrated over the entire beam pulse for each channel and recorded with the sign of the beam polarization. The number of Møller scattered electrons detected per pulse varies with current and target thickness, but is typically ten per pulse. Since the momenta and scattering angles of the Møller scatters are correlated, the scatters fall in a tilted stripe at the detector and are seen as an elastic scattering peak with a small radiative tail above an unpolarized background. After a data run, an average signal is calculated separately for the two beam helicities. An unpolarized signal and an asymmetry is computed from these quantities channel by channel. The background is fit to the wings of the distribution and subtracted from the region of the Møller peak. The observed asymmetry of the Møller signal is then related to the beam polarization by Eq. (13).

Behind the silicon detectors is a Pb-glass block array with seven 4-by-4-inch blocks above and below the bend plane. Both electrons from a Møller scatter are seen by looking for time coincidences between appropriate pairs of top and bottom blocks. The time resolution is ≈ 1 nsec, yielding sharp coincidence peaks with negligible background. The large size of the lead glass blocks contains all of the Møller lineshape; consequently, corrections for target electron momenta are $\leq 1\%$. The observed raw asymmetry of the coincidence pairs only needed small corrections for deadtime and acceptance. The results of the single- and double-arm

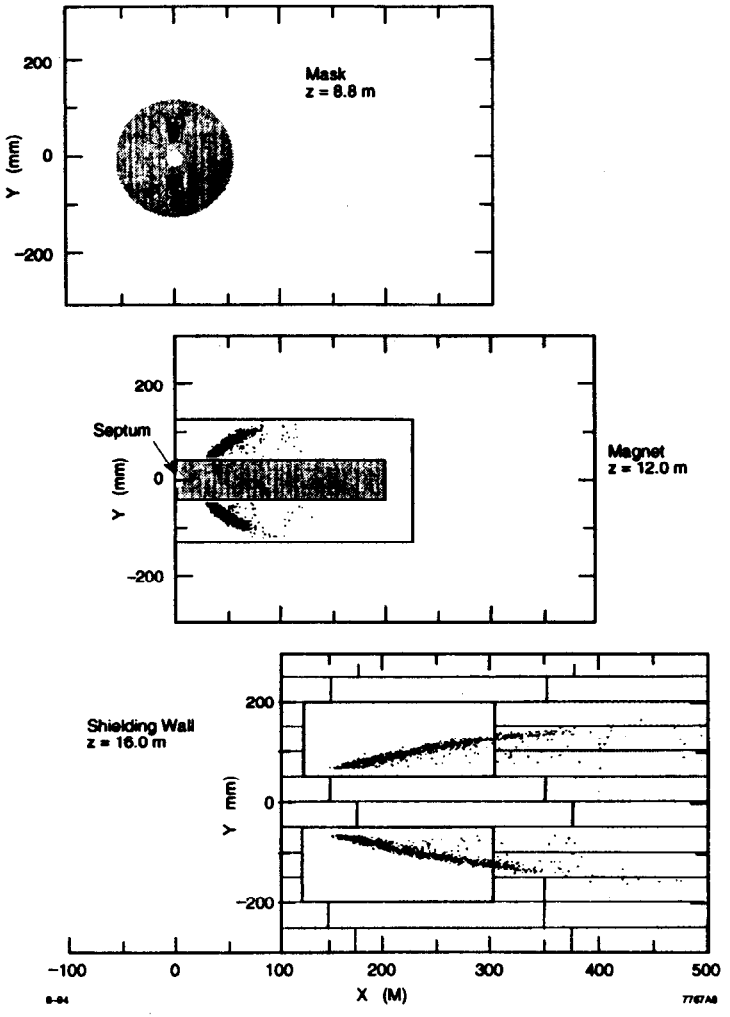

Figure 5: Spatial distribution of Møller scattered electrons at the mask (top), magnet exit (middle), and downstream momentum slit (bottom).

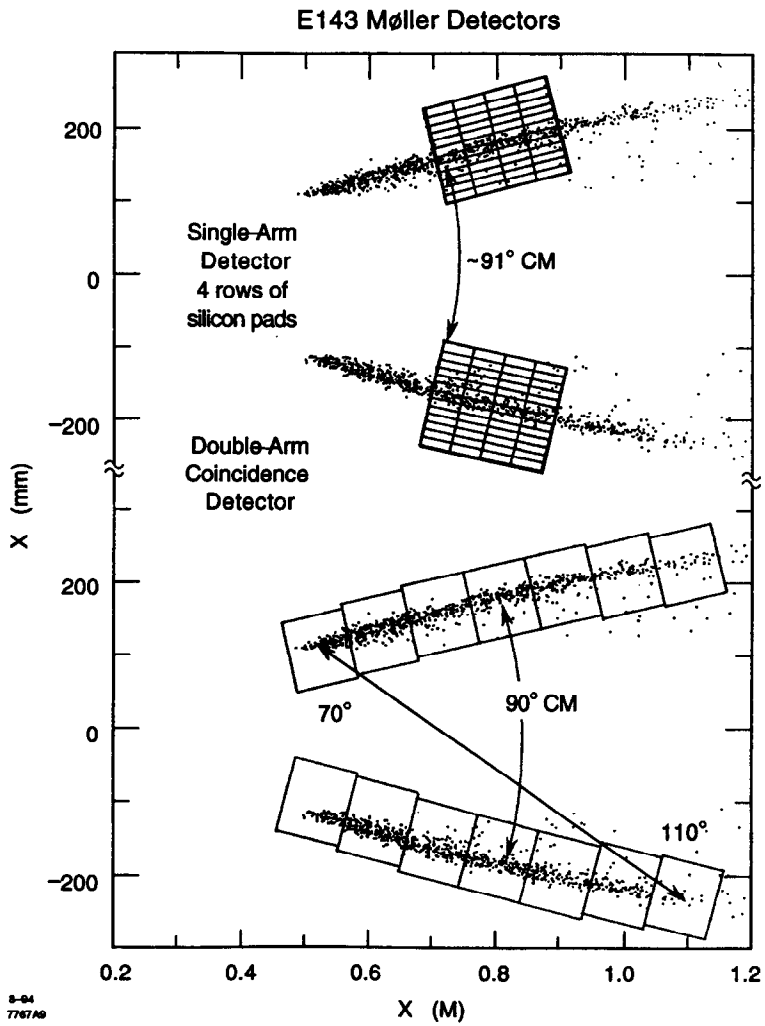

Figure 6: Single- and double-arm detector positions relative to the Møller scattered electrons.

measurements were in good agreement. The systematic error in the double-arm measurements was considerably smaller than the error in the single-arm detectors which had larger corrections and uncertainties for backgrounds and lineshape. The double-arm detector measurements are used throughout this paper.

Beam polarization measurements were made daily throughout E143 and were found to vary with the quantum efficiency (QE) of the SLAC polarized gun [Fig. 7(b)]. The measurements were fitted to an arbitrary functional form which was used to interpolate P_{beam} between Møller measurements using the frequent measurements of QE shown in Fig. 7(a). The measured values of 0.83–0.86 were in good agreement with other polarimeter measurements of beam from this type of photocathode. The spread of the daily measurements about the fitted P_{beam} versus QE function was somewhat larger than could be explained by statistics, either due to systematic errors in the Møller measurements or to nonreproducibility in the P versus QE behavior of the beam. Including all of these effects and the uncertainty in the foil polarization, the overall systematic error on the E143 beam polarization measurements was calculated to be 0.02.

2.3 Polarized Targets

Cryogenic ammonia and deuterated ammonia targets polarized by dynamic nuclear polarization provided the polarized protons and deuterons needed for this experiment. The polarized target assembly shown in Fig. 8 contained three target cells. The 3 cm long, 2.5 cm diameter porous target cylinders were filled with granules of either ammonia $^{15}NH_3$ (99.7% ^{15}N isotopic purity) or deuterated ammonia $^{15}ND_3$ (98% D isotopic purity), and immersed in a vessel filled with liquid He maintained at 1° K using a high-power evaporation refrigerator. Superconducting coils provided a uniform field of 4.8 T over the cell volume. A third, empty cell was used to measure scattering rates from the target cell walls, NMR coils, and cooling helium.

The target material was polarized by the technique of dynamic nuclear polarization. The ammonia granules were pre-irradiated[17] with 30 to 350 MeV electron beams to create a dilute assembly of paramagnetic radicals. During the experiment, the targets were exposed to 138 GHz microwaves to drive the hyperfine transition which aligns the nuclear spins with the magnetic field. This technique produced proton polarizations of 65 to 80% in ten to 20 minutes. Deuteron po-

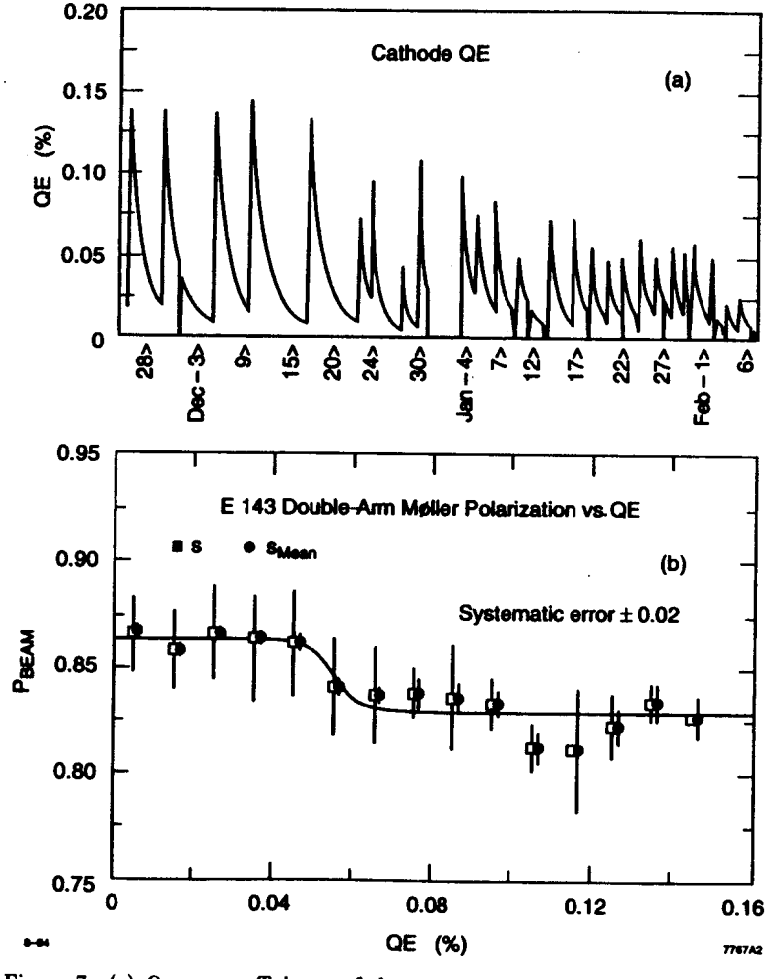

Figure 7: (a) Quantum efficiency of the source photocathode during the E143 experiment. (b) Beam polarization measured by the E143 Møller polarimeter double-arm detectors versus the quantum efficiency of the source photocathode. The fitted curve was used to interpolate between Møller polarization measurements.

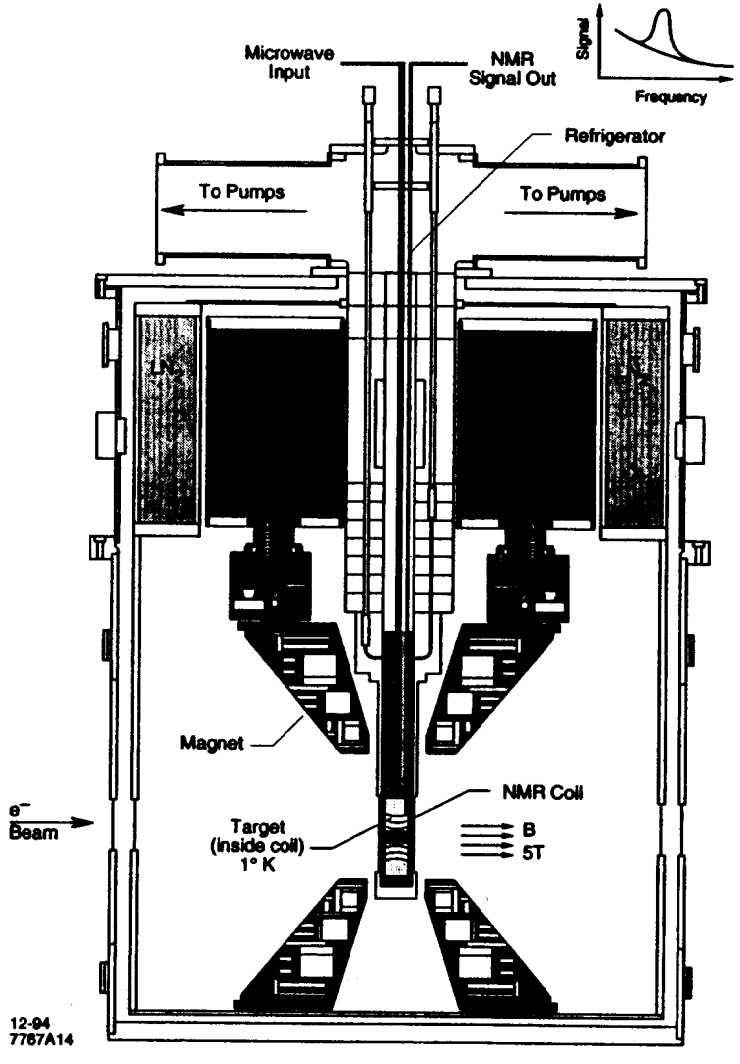

Figure 8: The E143 polarized target.

larizations of 25 to 40% were achieved with somewhat longer polarizing times. After exposure to the electron beam for eight to 12 hours, the proton polarization typically dropped to 50 to 55% due to radiation damage by the beam. Most of the radiation damage was repaired by annealing the target at about 80° K.

The electron beam was rastered over the 4.9 cm^2 front surface of the target to distribute beam heating and radiation damage uniformly. The rastering pattern was such that the beam returned to the same spot on the target only once per second, resulting in negligible local depolarization effects due to beam heating. After typically ten anneal cycles, the average polarization began to decline and the material was replaced. The target polarization direction was usually reversed after each anneal by adjusting the microwave frequency. Also, the direction of the magnetic field was reversed several times during the experiment. Approximately equal amounts of data were taken in each of the four polarization/field direction combinations, and the measured asymmetries were consistent for the four data samples.

The target polarization P_t was measured using a series LCR resonant circuit and Q-meter detector.[18] The inductance was supplied by an NMR coil embedded in the ammonia granules, calibrated by measuring the thermal-equilibrium (TE) signal near 1.6° K with beam and microwaves off. The results of these periodic calibrations for the ammonia targets is shown in Fig. 9. The total relative systematic error on P_t was 2.5% for the proton targets, dominated by the observed 2.2% rms spread in the TE measurements. The corresponding uncertainty for deuteron targets was 4% of P_t.

2.4 Spectrometers

The scattered electrons with energy E' between 6 and 25 GeV were detected in two independent magnetic spectrometers[19] positioned at angles of 4.5° and 7° with respect to the incident beam in the horizontal plane. The spectrometers shown in Fig. 10 were first used in the E142 experiment.[7] Electrons were distinguished from a background of pions in each spectrometer using two threshold gas Cherenkov counters and a 24-radiation-length shower-counter array composed of 200 lead-glass blocks. Seven planes of plastic scintillator hodoscopes were used to measure particle momenta and scattering angles.

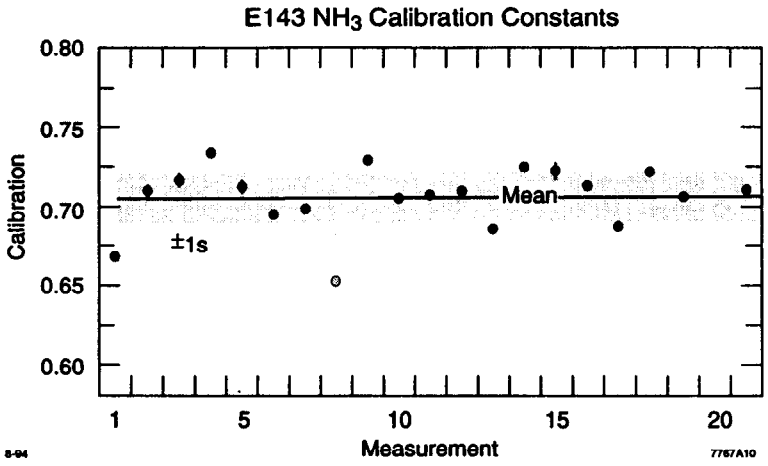

Figure 9: Results of thermal equilibrium measurements performed periodically on the proton targets to calibrate the NMR coils. The measured spread of these measurements was used to determine the systematic error of the NMR technique.

The design for both spectrometers utilizes two large aperture dipoles bending vertically with opposite polarity. The bend angles and magnet spacing were chosen to maximize electron acceptance over a large momentum range and to reject photon backgrounds. Soft or hard photons scattered from the target must bounce or shower at least twice from magnet or collimator edges before reaching any of the active detector elements. Lead collimators before and after the dipoles define the angular acceptance and provide fine tuning of the scattering rate into either spectrometer arm. The overall acceptance is ±10 milliradians in the nonbend (horizontal) plane in the 7° spectrometer and ±5 milliradians in the 4.5° spectrometer. The acceptence in the bend plane is correlated with momentum but is roughly ±14 milliradian in both arms.

Both the 2- and 4-meter-long Cherenkov detectors contained N_2 at partial atmospheric pressure. N_2 was chosen for its low scintillation and low cross-section properties. The gas pressures were set so pions below 9 GeV/c in the 2-meter and 13 GeV/c in the 4-meter would not emit Cherenkov light. Electrons of similar momentum were detected with $\geq$ 99% efficiency in the 2-meter Cherenkov and with $\geq$ 94% efficiency in the 4-meter Cherenkov.

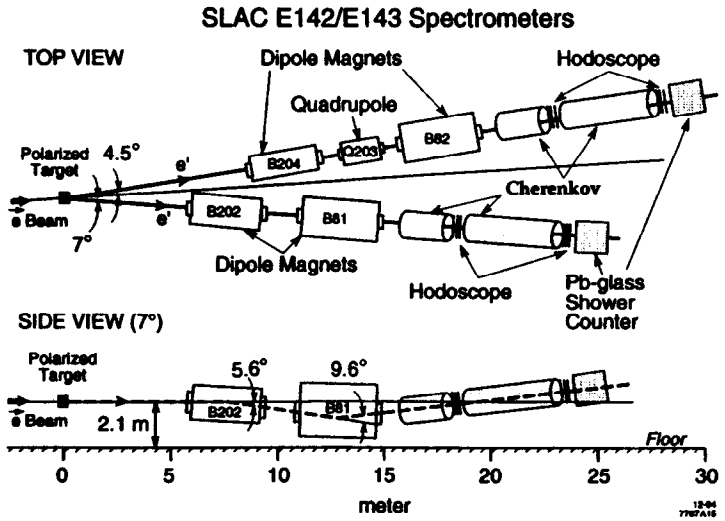

Figure 10: The E142/E143 spectrometers contain 4.5° and 7° arms operating in parallel. Each arm contains two dipole magnets, 2- and 4-meter-long threshold Cherenkov detectors, seven hodoscope planes, and a large lead-glass shower counter array.

In Fig. 11, the trajectories of rays of differing momenta and scattering angle are depicted with respect to the central trajectory ($E' = 12.5$ GeV/c, $\phi_x = \phi_y = 0$). The position and angle of the rays in the hodoscope arrays are correlated to the scattering angle and momentum of the observed electrons. The hodoscope arrays are made from 3 cm wide scintillator paddles overlapped with both nearest neighbors achieving a bin size of approximately 1 cm. Tracks were reconstructed by correlating scintillator hits in both time and space with an efficiency of over 92%. The achieved angular resolution on tracks was ± 0.3 mr in the nonbend plane and $\pm$ 0.7–0.9 mr in the bend plane. The momentum resolution varied with momentum from $\delta_p/p = 2.2\%$ at 18 GeV/c to 6.9% at 7 GeV/c.

The electron energy was measured in the lead-glass shower counters. The extruded $6 \times 6 \times 50$-cm lead-glass blocks, previously used in the ASP experiment,[20] were stacked in a ten wide by 20 high array. Electrons were identified by the pattern and magnitude of the energy deposition in the lead-glass array. The energy resolution was measured as $\sigma/E = \pm\ 7\%/\sqrt{E}$. Energy clusters were formed by combining shower hits above 200 MeV/c in neighboring blocks. Electrons were required to have an energy cluster matching an extrapolated hodoscope track to within 6.2 cm in x and y and within 10 nsec in time. Good electron tracks were also required to have momentum and energy measurements agreeing within 20%. The combination of the hodoscope and shower counter measurements were able to determine the x of the scattered electron to within 10% over the x range of 0.029 to 0.8.

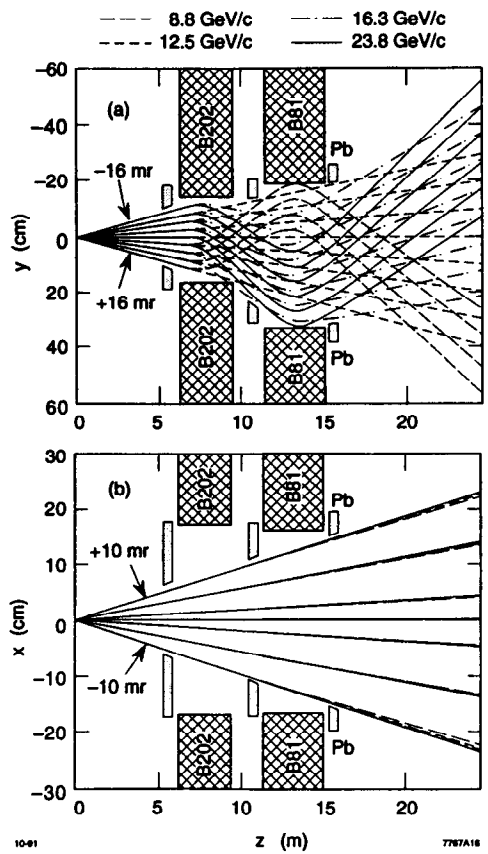

Figure 11: Electron trajectories of differing momenta and scattering angles in (a) the 7° spectrometer bend and (b) nonbend planes. Positions are drawn relative to the central ray of 12.5 GeV/c and nominal scattering angle.

3 Data Analysis

3.1 Data Set

The data collected by E143 are tabulated in Table 1. Over 200 million triggers were logged on proton and deuteron targets, primarily at an incident beam energy of 29.1 GeV. Data with lower beam energies of 16.2 and 9.8 GeV were taken to check the Q^2 dependence of the measured asymmetries. About 1/4 of the data was with the target spin oriented perpendicular to the incoming beam helicity to measure $A_\perp$ and g_2. Special runs were taken with empty target cells or reversed spectrometer magnet polarities to measure various contaminations in the electron signal. Data were also taken with aluminum and carbon targets to allow comparison of the measured cross section with previous experiments. The analysis in this paper uses only the data at 29.1 GeV.

3.2 Measured Asymmetries

Electron tracks satisfying the previously discussed analysis cuts were tabulated by target and beam helicity, beam energy, scattering angle, energy, x, Q^2, and incident charge. The counts were normalized by the incident charge on target and corrected for deadtime in the data acquisition system. The experimental longitudinal and transverse asymmetries $A_\parallel$ and $A_\perp$ were determined from

$$A_\parallel(\text{or}A_\perp) = \left(\frac{N_L - N_R}{N_L + N_R}\right)\frac{C}{f P_b P_t} + A_{RC}. \tag{14}$$

N_L and N_R are the corrected numbers of scattered electrons per incident charge for negative and positive beam helicity, respectively; C is a correction factor for the polarized nitrogen nuclei; f is the dilution factor representing the fraction of measured events originating from polarizable hydrogen or deuterium within the target; and A_{RC} is the radiative correction. The corrected rates N_R and N_L were adjusted for contributions from secondary sources (such as e^+/e^- pair production from photons) measured by reversing the spectrometer polarity. These processes showed no measurable asymmetry. The corrections to the rates were 10% at the lowest x bin and decreased rapidly at higher x. C was determined from measured ^{15}N polarizations and a shell-model calculation to determine the contribution of the unpaired p-shell proton. C was typically 0.98 for the proton (NH_3) target

E143 Data Summary

Target Field	Energy (GeV)	Target	Beam charge (electrons $\times 10^{15}$)	Electrons (triggers $\times 10^{6}$)
Longitudinal	29.13	$^{15}NH_3$	130	39
		$^{15}ND_3$	170	77
	16.20	$^{15}NH_3$	37	11
		$^{15}ND_3$	17	7.5
	9.8	$^{15}NH_3$	19	6
		$^{15}ND_3$	16	7
Transverse	29.13	$^{15}NH_3$	56	17
		$^{15}ND_3$	69	30
Either/none	all	C, Al, Empty	16	8
				2×10^{8}

Table 1: E143 data summary. The approximate charge on target and number of triggers logged are shown by energy and target type.

and 1.016 for the deuteron (ND_3) target. The deuterium data required an additional correction factor in Eq. (14) to correct for the polarization of the 2% NH_3 contamination in the ND_3 target.

3.3 Dilution Factor

The dilution factor f for the proton data varied with x between 0.13 and 0.17. It was determined from the number of measured counts expected from each component of the $^{15}NH_3$ target, which contained by weight about 13% free protons, 65% ^{15}N, 10% ^{4}He, 6% Al, 5% Cu, and 1% Ti. The relative systematic error in f ranged from 2.2% to 2.6%, as determined from uncertainties in the target composition and in the expected ratios of cross sections from different nuclei.

The deuteron target contained by weight about 23% deuterons, 56% ^{15}N, 10% ^{4}He, 6% Al, 4% Cu, and 1% Ti. The dilution factor was also x-dependent and varied from 0.22 at low x to 0.25 at high x. The relative systematic error in f was determined in a similar fashion and again ranged from 2.2% to 2.6%.

3.4 Radiative Corrections

The structure functions and sum rules are written at the Born level and assume that single photon exchange dominates the cross section. The measured cross sections and asymmetries, however, may contain sizable contributions from higher order internal radiative diagrams and from external radiation in the solid target. The primary effect of these processes is to move scattering events at a given E' and θ to lower E'. The radiative correction A_{RC} corrects for these effects and includes both internal[21] and external[22] contributions. The internal radiative corrections for both $A_\parallel$ and $A_\perp$ were evaluated using the formulae of Kukhto and Shumeiko.[21] The cross-section components of the asymmetry were "externally radiated" according to Tsai[22] to form the "fully radiated" asymmetry corrections A_{RC}. The correction varied slowly with x and typically changed $A_\parallel^p$ by $\leq 2\%$. The measured deuteron target asymmetries were small; consequently, A_{RC} changed the deuteron asymmetry by 10% of its value. Systematic errors on A_{RC} were estimated based on uncertainties in the input models used to fit the data and correspond to relative errors on A_{RC} for the proton targets of typically 2% for $x > 0.1$, increasing to 11% at $x = 0.03$.

4 Results

4.1 Proton Data at 29.1 GeV

From $A_\parallel$ and $A_\perp$, the ratio g_1^p/F_1^p was calculated using the definition in Eq. (1). The ratio of virtual photon total absorption cross sections $R = \sigma_L/\sigma_T$ was computed from a global fit[23] of world data. The ratio g_1/F_1 is related to the virtual photon longitudinal asymmetry $A_1 = (g_1/F_1) - \gamma^2(g_2/F_1)$, or $A_1 = d^{-1}\{A_\parallel(1 + \gamma^2 y/2) - \gamma^2 y A_\perp/[2\tan(\theta/2)]\}$, where $\gamma^2 = Q^2/\nu^2$. The approximation $A_1 = g_1/F_1$ is valid only when $\gamma \approx 0$ or $g_2 \approx 0$.

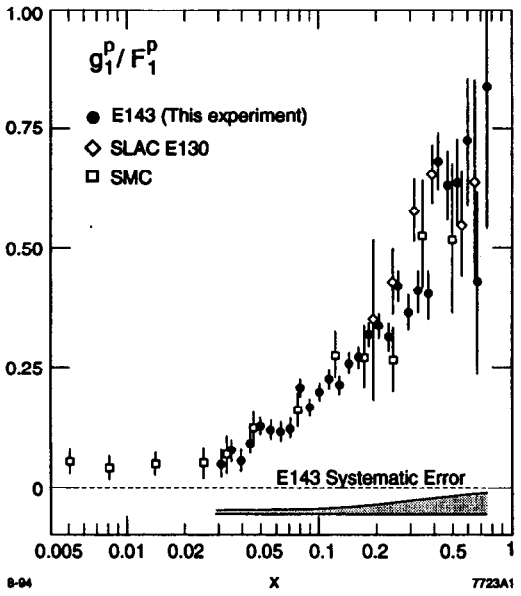

Figure 12: The ratio g_1^p/F_1^p measured by E143, and data from SLAC E130[2] and the CERN SMC experiment.[25]

The values of g_1^p/F_1^p from this experiment[24] at $E = 29.1$ GeV are tabulated in Table 2 and displayed in Fig. 12 along with the results of previous experiments. Data from the two spectrometers, which differ by about a factor of two in average Q^2, are consistent in the overlap region $0.07 < x < 0.55$ and therefore have been averaged together. The systematic errors include contributions from P_b, P_t, f, and A_{RC} discussed above, as well as 3 to 5% in d arising from the uncertainty in R.

It can be seen in Fig. 12 that both the previous SLAC data[2] and the higher Q^2 SMC data[25] ($< Q^2 >= 10$ (GeV/c)^2) are in agreement with the data of this experiment, indicating that to a good approximation, g_1^p/F_1^p is independent of Q^2 over the (x, Q^2) range where this ratio has been measured. The SLAC E130 data are plotted assuming $A_\perp = 0$ (the experiment measured $A_\parallel$ only), and the SMC data are plotted assuming $g_1/F_1 \approx A_1$, which is a good approximation at their beam energy of 190 GeV.

Table 2: Average values g_1^p/F_1^p from the $E = 29.1$ GeV data of this experiment at the indicated average values of Q^2. Also shown are values of g_1^p at fixed $Q^2 = 3$ (GeV/c)^2, evaluated assuming g_1^p/F_1^p is independent of Q^2.

x	$<Q^2>$ (GeV/c)^2	g_1^p/F_1^p ±stat. ±sys.	g_1^p at $Q^2 = 3$ (GeV/c)^2 ±stat. ±sys.
0.031	1.27	$0.048 \pm 0.029 \pm 0.008$	$0.223 \pm 0.132 \pm 0.040$
0.035	1.39	$0.075 \pm 0.022 \pm 0.008$	$0.308 \pm 0.092 \pm 0.037$
0.039	1.52	$0.055 \pm 0.021 \pm 0.008$	$0.203 \pm 0.077 \pm 0.034$
0.044	1.65	$0.091 \pm 0.020 \pm 0.008$	$0.295 \pm 0.066 \pm 0.031$
0.049	1.78	$0.127 \pm 0.020 \pm 0.008$	$0.366 \pm 0.058 \pm 0.028$
0.056	1.92	$0.117 \pm 0.020 \pm 0.008$	$0.300 \pm 0.052 \pm 0.024$
0.063	2.07	$0.114 \pm 0.020 \pm 0.009$	$0.258 \pm 0.046 \pm 0.021$
0.071	2.22	$0.122 \pm 0.020 \pm 0.010$	$0.245 \pm 0.041 \pm 0.019$
0.079	2.49	$0.205 \pm 0.020 \pm 0.011$	$0.368 \pm 0.036 \pm 0.017$
0.090	2.79	$0.164 \pm 0.020 \pm 0.012$	$0.263 \pm 0.032 \pm 0.015$
0.101	3.11	$0.199 \pm 0.020 \pm 0.013$	$0.284 \pm 0.029 \pm 0.014$
0.113	3.40	$0.225 \pm 0.021 \pm 0.014$	$0.287 \pm 0.027 \pm 0.014$
0.128	3.71	$0.212 \pm 0.022 \pm 0.014$	$0.242 \pm 0.025 \pm 0.013$
0.144	4.03	$0.260 \pm 0.023 \pm 0.014$	$0.265 \pm 0.023 \pm 0.013$
0.162	4.38	$0.273 \pm 0.024 \pm 0.015$	$0.249 \pm 0.022 \pm 0.012$
0.182	4.73	$0.318 \pm 0.025 \pm 0.016$	$0.258 \pm 0.020 \pm 0.012$
0.205	5.06	$0.336 \pm 0.027 \pm 0.018$	$0.242 \pm 0.019 \pm 0.012$
0.230	5.41	$0.313 \pm 0.029 \pm 0.020$	$0.199 \pm 0.019 \pm 0.012$
0.259	5.73	$0.419 \pm 0.033 \pm 0.023$	$0.233 \pm 0.018 \pm 0.012$
0.292	6.05	$0.363 \pm 0.037 \pm 0.026$	$0.174 \pm 0.018 \pm 0.011$
0.328	6.40	$0.409 \pm 0.043 \pm 0.028$	$0.167 \pm 0.017 \pm 0.010$
0.370	6.72	$0.403 \pm 0.049 \pm 0.030$	$0.137 \pm 0.017 \pm 0.009$
0.416	7.06	$0.679 \pm 0.058 \pm 0.032$	$0.187 \pm 0.017 \pm 0.008$
0.468	7.37	$0.630 \pm 0.071 \pm 0.034$	$0.138 \pm 0.016 \pm 0.007$
0.526	7.64	$0.635 \pm 0.088 \pm 0.036$	$0.109 \pm 0.015 \pm 0.007$
0.592	8.92	$0.722 \pm 0.133 \pm 0.038$	$0.095 \pm 0.018 \pm 0.007$
0.666	9.05	$0.428 \pm 0.192 \pm 0.040$	$0.041 \pm 0.019 \pm 0.007$
0.749	9.18	$0.837 \pm 0.300 \pm 0.043$	$0.052 \pm 0.019 \pm 0.008$

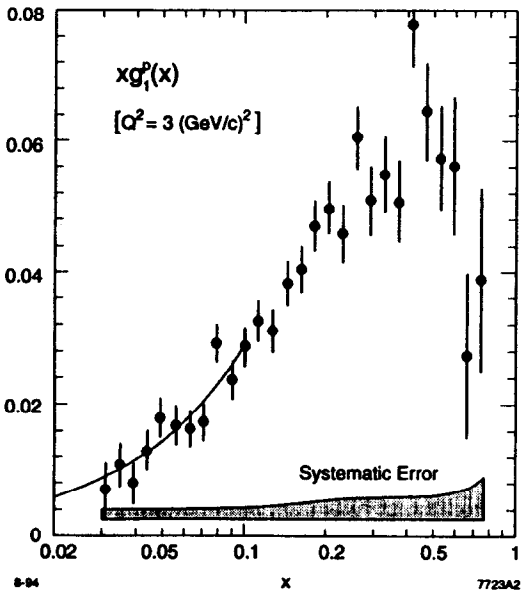

Figure 13: xg_1^p versus x as measured by E143. The error bars are statistical only. The size of the systematic error is shown by the shaded bar and is always smaller than the statistical error.

Values of xg_1^p at the average $Q^2 = 3$ (GeV/c)^2 of this experiment are shown in Fig. 13. The evaluation at constant Q^2 is model-dependent, and we have made the assumption that g_1^p/F_1^p depends only on x (Ref. 26). For $F_1^p = (1+\gamma^2)F_2^p/[2x(1+R)]$, we used the NMC fit[27] to F_2^p and the SLAC fit[23] to R. Using the SLAC global fit[28] to F_2^p gives similar results. The systematic errors on g_1^p include an x-dependent error on the ratio F_1^p/d which varies from 2.5% in the mid-x range to 4% at low x and 10% at high x. The integral of g_1^p over the measured range $0.029 < x < 0.8$ is proportional to the area under the data points in Fig. 13, yielding $\int_{0.029}^{0.8} g_1^p(x)dx = 0.120 \pm 0.004 \pm 0.008$, where the first error is statistical, and the second is systematic. The value of the integral is decreased by 0.006 if g_1 is computed from A_1 and A_2, and both A_1 and A_2 are assumed independent of Q^2 instead of assuming that g_1/F_1 is independent of Q^2.

An extrapolation from $x = 0.8$ to $x = 1$ was done assuming g_1 is proportional to $(1-x)^3$ at high x (Ref. 29); this yields $\int_{0.8}^{1} g_1^p(x)dx = 0.001 \pm 0.001$. The extrapolation to $x = 0$ is more model dependent. The data for $x < x_{max}$ were fit using the Regge motivated form[30] $g_1^p = Cx^{-\alpha}$, where α was restricted to the range[31] $-0.5 < \alpha < 0$, and the results are $\int_0^{0.029} g_1^p(x)dx = 0.006 \pm 0.006$. The error includes a statistical component, the uncertainty in α, and the effect of varying the fitting range from $x_{max} = 0.03$ (for which only SMC and EMC data contribute) to $x_{max} = 0.12$ (for which the present data dominate). The fit for $\alpha = 0$ and $x_{max} = 0.1$ is shown in Fig. 2. An alternate functional form[32] $g_1^p = C\ln(1/x)$, which provides a good fit to the low-x F_2 data from NMC and HERA, leads to $\int_0^{0.029} g_1^p(x)dx = 0.013 \pm 0.003$.

Assuming that g_1/F_1 depends only on x and that g_1^p follows the Regge form at low x, the total integral is $\Gamma_1^p = 0.127 \pm 0.004 \pm 0.010$. This is in good agreement with the value from SMC,[25] $\Gamma_1^p = 0.122 \pm 0.011 \pm 0.011$, obtained at $Q^2 = 3$ (GeV/c)^2 assuming $g_1/F_1 \approx A_1$ is independent of Q^2. Our result is considerably lower (by 2.7 sigma) than the Ellis-Jaffe sum rule prediction of $\int g_1^p = 0.160 \pm 0.006$ from Eq. (6).

4.2 Deuteron Data

The deuteron data from the two spectrometers are also consistent with A_1^d, A_2^d, and g_1^d/F_1^d being independent of Q^2 in the overlap region $0.07 < x < 0.5$, and were averaged together. The values of A_1^d from this experiment at $E = 29.1$ GeV (Ref. 33) shown in Fig. 14 and listed in Table 3 are consistent with earlier, less precise results from the SMC Collaboration.[6]

Values of g_1^d at the average $Q^2 = 3$ (GeV/c)^2 of this experiment are shown in Fig. 15(a). The evaluation of g_1^d at constant Q^2, as in the proton, is model dependent and was made assuming that g_1^d/F_1^d depends only on x. The systematic error on F_1^d is typically 2.5%, increasing to 5% at the lowest x bin and 15% at the highest x bin. The integral of g_1^d at $Q^2 = 3$ (GeV/c)^2 and over the measured range $0.029 < x < 0.8$ is $\int_{0.029}^{0.8} g_1^d(x)dx = 0.041 \pm 0.004 \pm 0.004$. The integral is decreased by 0.003 if we make an alternate assumption that both A_1^d and A_2^d are independent of Q^2.

Assuming g_1^d varies as $(1-x)^3$, the extrapolation for $x > 0.8$ yields $\int_{0.8}^{1} g_1^d(x)dx = 0.000 \pm 0.001$. Fitting the data to the Regge-motivated form gives $\int_0^{0.029} g_1^d(x)dx =$

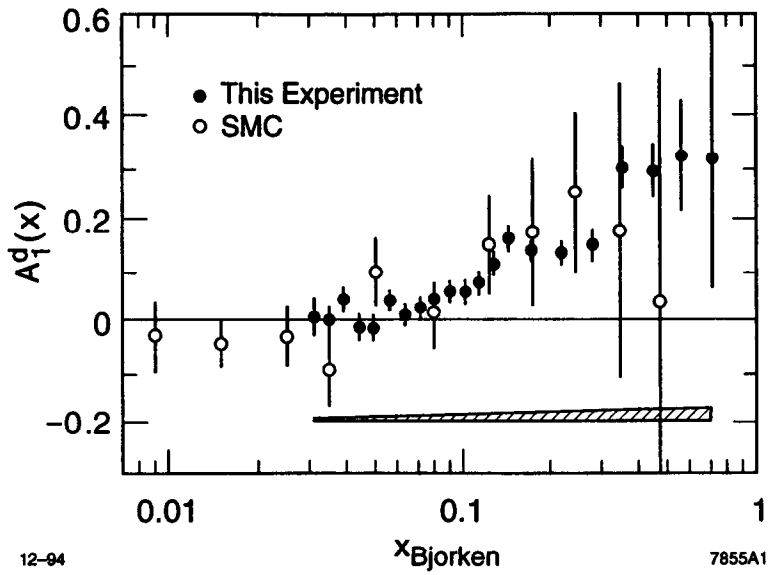

Figure 14: The virtual photon asymmetry, A_1^d, from this experiment. The systematic errors are indicated by the shaded band. The average Q^2 varies from 1.3 (GeV/c)^2 at low x to 10 (GeV/c)^2 at high x. Data from the SMC Collaboration[6] are also shown.

Table 3: Average values A_1^d from the $E = 29.1$ GeV data of this experiment at the indicated average values of Q^2. Also shown are values of g_1^d at fixed $Q^2 = 3$ (GeV/c)^2, evaluated assuming g_1^d/F_1^d is independent of Q^2.

x	$<Q^2>$ (GeV/c)^2	A_1^d ±stat. ±sys.	g_1 at $Q^2 = 3$ (GeV/c)^2 ±stat. ±sys.
0.031	1.27	$0.012 \pm 0.026 \pm 0.000$	$0.055 \pm 0.116 \pm 0.000$
0.035	1.39	$0.018 \pm 0.021 \pm 0.000$	$0.069 \pm 0.083 \pm 0.000$
0.039	1.52	$0.062 \pm 0.020 \pm 0.000$	$0.216 \pm 0.071 \pm 0.000$
0.044	1.65	$0.016 \pm 0.020 \pm 0.000$	$0.050 \pm 0.063 \pm 0.000$
0.049	1.78	$0.031 \pm 0.020 \pm 0.000$	$0.084 \pm 0.056 \pm 0.000$
0.056	1.92	$0.023 \pm 0.021 \pm 0.000$	$0.056 \pm 0.051 \pm 0.000$
0.063	2.07	$0.040 \pm 0.021 \pm 0.000$	$0.085 \pm 0.045 \pm 0.000$
0.071	2.22	$0.050 \pm 0.022 \pm 0.000$	$0.094 \pm 0.041 \pm 0.000$
0.079	2.50	$0.071 \pm 0.022 \pm 0.000$	$0.118 \pm 0.036 \pm 0.000$
0.090	2.80	$0.062 \pm 0.022 \pm 0.000$	$0.093 \pm 0.032 \pm 0.000$
0.101	3.11	$0.067 \pm 0.022 \pm 0.000$	$0.088 \pm 0.029 \pm 0.000$
0.113	3.42	$0.077 \pm 0.023 \pm 0.000$	$0.090 \pm 0.027 \pm 0.000$
0.128	3.73	$0.125 \pm 0.024 \pm 0.000$	$0.129 \pm 0.025 \pm 0.000$
0.144	4.05	$0.148 \pm 0.025 \pm 0.000$	$0.135 \pm 0.023 \pm 0.000$
0.162	4.39	$0.086 \pm 0.027 \pm 0.000$	$0.070 \pm 0.022 \pm 0.000$
0.182	4.73	$0.210 \pm 0.029 \pm 0.000$	$0.149 \pm 0.020 \pm 0.000$
0.205	5.08	$0.142 \pm 0.031 \pm 0.000$	$0.089 \pm 0.019 \pm 0.000$
0.230	5.42	$0.129 \pm 0.034 \pm 0.000$	$0.070 \pm 0.019 \pm 0.000$
0.259	5.74	$0.200 \pm 0.038 \pm 0.000$	$0.094 \pm 0.018 \pm 0.000$
0.292	6.07	$0.216 \pm 0.044 \pm 0.000$	$0.087 \pm 0.018 \pm 0.000$
0.328	6.41	$0.249 \pm 0.051 \pm 0.000$	$0.084 \pm 0.017 \pm 0.000$
0.370	6.75	$0.281 \pm 0.060 \pm 0.000$	$0.078 \pm 0.016 \pm 0.000$
0.416	7.06	$0.219 \pm 0.071 \pm 0.000$	$0.048 \pm 0.016 \pm 0.000$
0.468	7.35	$0.336 \pm 0.088 \pm 0.000$	$0.058 \pm 0.015 \pm 0.000$
0.526	7.59	$0.382 \pm 0.110 \pm 0.000$	$0.050 \pm 0.015 \pm 0.000$
0.592	8.92	$0.200 \pm 0.172 \pm 0.000$	$0.020 \pm 0.017 \pm 0.000$
0.666	9.06	$0.614 \pm 0.252 \pm 0.000$	$0.043 \pm 0.017 \pm 0.000$
0.749	9.18	$0.212 \pm 0.394 \pm 0.000$	$0.009 \pm 0.017 \pm 0.000$

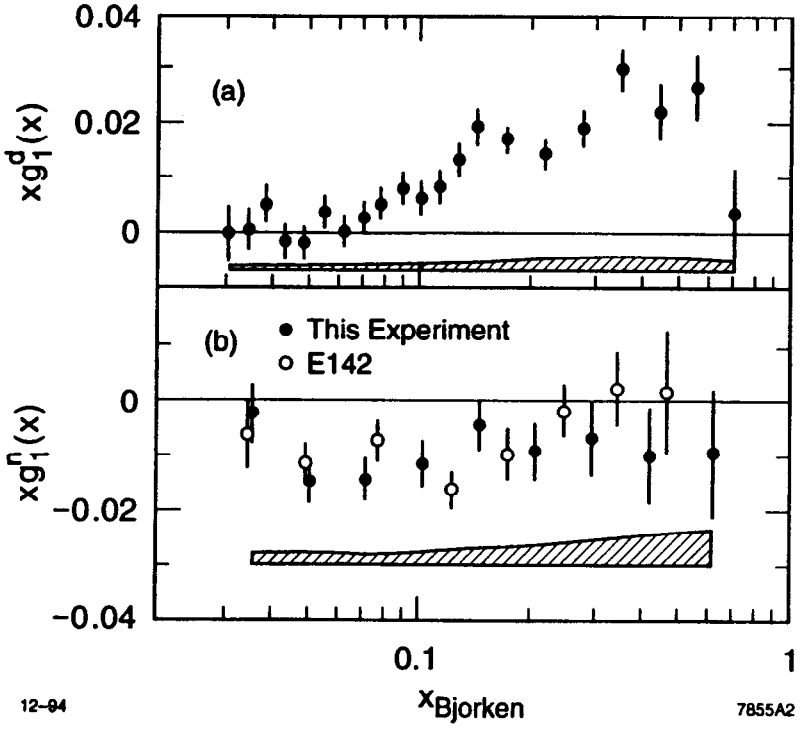

Figure 15: The variable xg_1^n from this experiment (E143) as a function of x for (a) the deuteron and (b) the neutron. The errors are statistical only. Systematic errors are indicated by the shaded bands. Also shown are neutron data from SLAC E142.

0.001 ± 0.001. The uncertainty is calculated in a similar manner to the proton data. The alternate form $g_1^d(x) = C' \log(x)$ gives similar results. The Ellis-Jaffe sum rule predicts $\Gamma_1^d = 0.068 \pm .005$ where the measured value is $\Gamma_1^d(E143) = 0.043 \pm 0.004(\text{stat.}) \pm 0.004(\text{sys.})$, a 3.3 σ discrepancy. This measurement of Γ_1^d is the most precise test of the Ellis-Jaffe sum rule to date. This result is also consistent with the results of SMC:[6] $\Gamma_1^d(\text{SMC}) = 0.023 \pm 0.020(\text{stat.}) \pm 0.015(\text{sys.})$.

4.3 Neutron Data

The neutron spin structure function can be extracted using the relation $g_1^p(x) + g_1^n(x) = 2g_1^d(x)/(1 - 1.5\ \omega_D)$, where $\omega_D = 0.058$[12] is the probability for the deuteron to be in a D-state. The results obtained using our measurements of $g_1^d(x)$ and $g_1^p(x)$ (Ref. 24) are compared in Fig. 15(b) with the results obtained by E142 (Ref. 7) using a ^{3}He target. Using the same extrapolation procedure as in the case of the deuteron, we find $\Gamma_1^n(E143) = -0.035 \pm 0.010(\text{stat.}) \pm 0.011(\text{sys.})$, compared with $\Gamma_1^n(E142) = -0.022 \pm 0.007(\text{stat.}) \pm 0.009(\text{sys.})$. The correlations between proton and deuteron measurements were accounted for when determining the systematic uncertainty. The Ellis-Jaffe sum rule prediction for the neutron from Eq. (8) is $\int g_1^n = -0.011 \pm 0.005$.

4.4 Bjorken Sum Rule

The Bjorken sum rule prediction can be tested by combining proton and deuteron results: $g_1^p(x) - g_1^n(x) = 2g_1^p(x) - 2g_1^d(x)/(1 - 1.5\omega_D)$. At $Q^2 = 3$ (GeV/c)^2, $\Gamma_1^p(E143) - \Gamma_1^n(E143) = 0.164 \pm 0.011(\text{stat.}) \pm 0.017(\text{sys.})$. This result is consistent with that obtained by combining the Γ_1^p result from this experiment[24] and the Γ_1^n result from E142 (Ref. 7): $\Gamma_1^p(E143) - \Gamma_1^n(E142) = 0.151 \pm 0.008(\text{stat.}) \pm 0.013(\text{sys.})$. Both determinations of the Bjorken sum rule are consistent with the prediction of $\Gamma_1^p - \Gamma_1^n = 0.171 \pm 0.008$ at 3 (GeV/c)^2. Combining with SMC deuteron data[6] gives a result that is also in agreement with the prediction, within larger errors.

4.5 Net Quark Helicity

The proton and deuteron integrals can be used individually within the quark parton model to extract the contributions to the nucleon helicity of each type of quark and antiquark using Eq. (10). If the Bjorken sum rule is satisfied, the computed

fractions should be consistent for both targets. Substituting the measured proton integral into Eq. (10), we find that the fraction of the nucleon helicity carried by the quarks is $\Delta q = 0.29 \pm 0.10$. The fraction carried by strange quarks and antiquarks is $\Delta s = -0.10 \pm 0.04$. If the analogous formulae for the deuteron are used with the measured deuteron results, we find $\Delta q = 0.35 \pm 0.05$ and $\Delta s = -0.08 \pm 0.03$ in good agreement with the proton-derived result. A value of $\Delta q = 0.58$ is predicted by the Ellis-Jaffe sum rule. Averaging the E143 proton and deuteron results, the net quark helicity is found to be $\Delta q = 0.34 \pm 0.04$ and the net strange quark helicity is found to be $\Delta s = -0.09 \pm 0.02$. These results are considerably more precise than earlier determinations by EMC[5] (proton) $\Delta q = 0.12 \pm 0.17$, SMC[6] (deuteron) $\Delta q = 0.06 \pm 0.25$, SMC[25] (proton) $\Delta q = 0.22 \pm 0.14$, and E142[7] (neutron) $\Delta q = 0.57 \pm 0.11$ where the reported statistical and systematic errors have been added in quadrature. Fortuitously, a weighted average of the EMC, SMC, and E142 results also yield $\Delta q = 0.34 \pm 0.08$.

5 Summary

In conclusion, E143 has made high statistics measurements of the proton and deuteron spin structure functions g_1^p and g_1^d with considerably smaller statistical errors than previous electron scattering experiments at SLAC[1,2] and muon scattering experiments at CERN.[5,25] The data violate the predictions of the Ellis-Jaffe sum rule at the 2–3 sigma level, confirming the earlier, less precise results. Combining the proton and deuteron measurements, the difference $\Gamma_1^p - \Gamma_1^n$ is in good agreement with the fundamental Bjorken sum rule. Interpreting the results in the QPM, the data imply that 0.34 ± 0.04 of the proton helicity is carried by the quarks.

6 Future Experiments

E143 is continuing analysis of the proton and deuteron data with results for g_2^p and g_2^d expected soon. The Q^2 dependence of g_1 is also under study, utilizing the data taken at lower beam energies, and should be available in 1995. SLAC is presently upgrading the beam transport line into ESA to allow the delivery of 50 GeV polarized beams. SLAC E154 will take data in the fall of 1995 with a gaseous ^{3}He target to measure the neutron spin structure functions at lower x and higher x and Q^2 than E142. In 1996, SLAC E155 will reuse the E143 cryogenic target at the higher beam energy to extend the present measurements in x and Q^2. New spectrometers will be built jointly by the two experiments to exploit the new kinematics and to accommodate the expected higher rates. Since the average Q^2 of the new experiments, $Q^2 = 5(\mathrm{GeV/c})^2$, will be substantially higher than E142 ($Q^2 = 2(\mathrm{GeV/c})^2$ or E143 ($Q^2 = 3(\mathrm{GeV/c})^2$, comparison of the measured structure functions will test the importance of nonperturbative QCD (twist) effects which are expected to scale like $1/Q^2$. Establishing that the measured structure functions obey the scaling assumptions of Bjorken and Ellis-Jaffe would greatly simplify the theoretical interpretation of these results.

Elsewhere, the SMC collaboration will take further data with deuteron targets in 1995-1996. The HERMES experiment will start operation in 1995 using polarized hydrogen, deuterium, and ^{3}He gas jet targets in the electron storage ring at HERA. The use of gas jet targets greatly improves the dilution factor reducing systematic uncertainty. A large acceptance forward spectrometer will tag outgoing electrons and hadronic particles for detailed polarization studies. HERMES will operate parasitically with the HERA operation and should be able to accumulate high statistics for each of the different targets at beam energies ≤ 30 GeV.

Acknowledgments

I would like to thank my E143 colleagues for the use of their figures and descriptions of the E143 experiment. I thank my Wisconsin colleagues Jim Johnson and Richard Prepost for helpful discussions concerning this paper.

References

[1] SLAC E80, M. J. Alguard *et al.*, Phys. Rev. Lett. **37**, 1261 (1976); **41**, 70 (1978).

[2] SLAC E130, G. Baum *et al.*, Phys. Rev. Lett. **51**, 1135 (1983).

[3] J. D. Bjorken, Phys. Rev. **148**, 1467 (1966); Phys. Rev. D **1**, 1376 (1970).

[4] J. Ellis and R. L. Jaffe, Phys. Rev. D **9**, 1444 (1974); D **10**, 1669 (1974).

[5] EMC, J. Ashman *et al.*, Phys. Lett. **B206**, 364 (1988); Nucl. Phys. **B328**, 1 (1989).

[6] SMC, B. Adeva *et al.*, Phys. Lett. **B302**, 533 (1993).

[7] SLAC E142, P. L. Anthony *et al.*, Phys. Rev. Lett. **71**, 959 (1993).

[8] Particle Data Group, L. Montanet *et al.*, "Review of Particle Properties," Phys. Rev. **D50** (1994).

[9] S. A. Larin and J. A. M. Vermaseren, Phys. Lett. **B259**, 345 (1991) and references therein.

[10] M. S. Schmelling and R. D. St. Denis, Phys. Lett. **B329**, 323 (1994); S. Narison, Report No. CERN/TH.7188/94.

[11] S. Larin, Phys. Lett. **B334**, 192 (1994); A. L. Kataev, Report No. CERN-TH-7427/94.

[12] M. Lacombe *et al.*, Phys. Lett. **B250**, 139 (1981).

[13] T. Maruyama, E. Garwin, R. Prepost, and G. Zapalac, Phys. Rev. B **46**, 4261 (1992); R. Alley *et al.*, Report No. SLAC-PUB-6489 (1994).

[14] H. R. Band, Report No. WISC-EX-94-341 (1994).

[15] C. Møller, Ann. Phys. **14**, 532 (1932).

[16] L.G. Levchuk, Nucl. Instrum. Methods **A345**, 496 (1994).

[17] D. G. Crabb *et al.*, Phys. Rev. Lett. **64**, 2627 (1990); W. Meyer *et al.*, Nucl. Instrum. Methods **215**, 65 (1983).

[18] G. R. Court *et al.*, Nucl. Instrum. Methods **A324**, 433 (1993).

[19] G. G. Petratos *et al.*, Report No. SLAC–PUB–5678 (1991).

[20] G. T. Bartha *et al.*, Nucl. Instrum. Methods **275**, 59 (1989).

[21] T. V. Kukhto and N. M. Shumeiko, Nucl. Phys. **B219**, 412 (1983); N. Shumeiko, private communication for correction of misprints.

[22] Y. S. Tsai, Report No. SLAC-PUB-848, 1971; Y. S. Tsai, Rev. Mod. Phys. **46**, 815 (1974).

[23] L. W. Whitlow *et al.*, Phys. Lett. **B250**, 193 (1990).

[24] SLAC E143, K. Abe *et al.*, Phys. Rev. Lett. **74**, 346 (1995); Report No. SLAC–PUB–6508 (1994).

[25] SMC, D. Adams *et al.*, Phys. Lett. **B329**, 399 (1994).

[26] G. Altarelli, P. Nason, and G. Ridolfi, Phys. Lett. **B320**, 152 (1994).

[27] NMC, P. Amaudruz *et al.*, Phys. Lett. **B295**, 159 (1992).

[28] L. W. Whitlow *et al.*, Phys. Lett. **B282**, 475 (1992).

[29] S. J. Brodsky, M. Burkardt, and I. Schmidt, Report No. SLAC-PUB-6087 (1994).

[30] R. L. Heimann, Nucl. Phys. **B64**, 429 (1973).

[31] J. Ellis and M. Karliner, Phys. Lett. **B313**, 131 (1993).

[32] S. D. Bass and P. V. Landshoff, Report No. DAMTP 94/50 (1994); F. E. Close and R. G. Roberts, Report No. RAL-94-071 (1994).

[33] SLAC E143, K. Abe *et al.*, Report No. SLAC–PUB–6734 (1994).